Acta Mech 229, 1229–1250 (2018)
https://doi.org/10.1007/s00707-017-2049-3

ORIGINAL PAPER

F. Fusi · P. M. Congedo · A. Guardone · G. Quaranta

Shape optimization under uncertainty of morphing airfoils

Received: 7 May 2017 / Revised: 16 September 2017 / Published online: 13 November 2017

Abstract This paper is devoted to the formulation of a novel optimization under uncertainty framework for the definition of optimal shapes for morphing airfoils, applied here to advancing/retreating 2D airfoils. In particular, the morphing strategy is conceived with the intent of changing the shape at a given frequency to enhance aerodynamic performance. The optimization of morphing airfoils presented here only takes into account the aerodynamic performance. The paper is then focused on an aerodynamic optimization to set the optimal shape with respect to performance, where technological aspects are inserted through geometrical constraints. In fact, this paper presents an exploratory work on morphing geometries which aims at understanding the relationship between shape degree of freedom and actual aerodynamic gain. Thus, exploring and demonstrating the gain of the aerodynamic shape may drive the development of new mechanism for the realization of morphing structures, which could be applied to helicopter rotor blades.

1 Introduction

Aerodynamic forces to fly a helicopter are generated by the rotor, a system of rotating wings, called blades, that provide the lift to sustain flight, the propulsive force to move the aircraft through the air, and the control to trim the aircraft or change its attitude. In classical configurations, a single main rotor is employed, and a sideward tail rotor is required to provide anti-torque and directional control. The presence of rotating elements no doubt increases the complexity of helicopters from both aerodynamic and mechanic points of view. With regard to aerodynamics, the flowfield around the helicopter is dominated by unsteady, three-dimensional effects and interactions among the helicopter bodies (rotor blades, main body, and tail), as well as by vortices and wakes (see Fig. 1). This system is so complicated that, after many years of studies, it still defies an adequate and comprehensive description [22]. From a mechanic point of view, the presence of the rotor introduces the structural dynamics associated with the degrees of freedom of each blade. In conventional rotors with fully articulated hubs, helicopter blades are connected to the shaft by means of hinges which permit flap and lead-lag

F. Fusi · A. Guardone · G. Quaranta
Department of Aerospace Science and Technology, Politecnico di Milano, Via La Masa 34, 20156 Milan, Italy
E-mail: francesca.fusi@polimi.it

A. Guardone
E-mail: alberto.guardone@polimi.it

G. Quaranta
E-mail: giuseppe.quaranta@polimi.it

P. M. Congedo (✉)
Team CARDAMOM, INRIA Bordeaux Sud-Ouest, 33405 Talence Cedex, France
E-mail: pietro.congedo@inria.fr

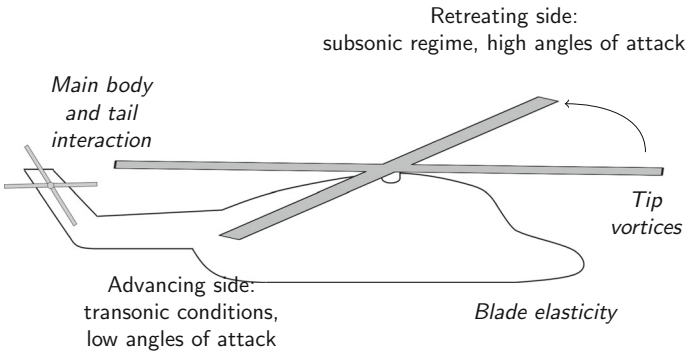

Fig. 1 Characteristics of the complex flowfield around a helicopter rotor in forward flight

motions. Pilot control is exerted by a change in the pitch angle of the blades, either cyclically or collectively. In addition, blades are slender bodies undergoing twisting and bending. The aeroelastic degrees of freedom, together with the remaining rigid motions, are coupled with the aerodynamic loads.

The aerodynamic flowfield, the blade dynamics and aeroelasticity, the pilot control are all relevant aspects of the environment surrounding the rotor, which must be taken into account in helicopter rotor design. This poses a great challenge to rotor designers, because the high-fidelity analysis of all these aspects and their mutual interaction requires the employment of tools with prohibitive cost. In comprehensive rotor analysis models, parsimonious models of each sub-system (e.g., aerodynamics, structural dynamics) are used to limit the cost necessary to estimate loads, displacements, and overall performance of the rotor [22, p. 805]. Examples are the CAMRAD II code developed by Johnson [14,15] or MBDyn [25,26] developed at the Department of Aerospace Science and Technology of the Politecnico di Milano. A modest cost permits parametric calculations that are crucial in the design stage. To some extent, the employment of cheap models and the combined use of models of different fidelity are intrinsically rooted in the design of rotors.

Another major challenge of rotor design is the definition of the performance goals. In fact, helicopter rotors are required to fulfill many different mission requirements. This translates into the necessity for rotor blades to operate with satisfactory performance in extremely different operating conditions, depending on the flight condition, pitch control, and advancing or climbing velocity.

In such a context, the goal of aerodynamic design is to improve the overall performance of the rotor by increasing thrust to accommodate for an increased payload, reducing the torque due to aerodynamic drag at a given thrust level, alleviating aerodynamic loads on the blade structure, enlarging the helicopter rotor flight envelope, and reducing vibrations.

Airfoils of helicopter rotor blades are required to operate in different conditions, and good performance in one condition does not transfer to another one. A very attractive solution to this problem is the employment of a blade capable of changing its shape during flight, that is a morphing blade.

With regard to helicopters, morphing rotor design is a challenging and active area of research [4]. In helicopter applications, the urgent need to improve the boundaries of the flight envelope leads research and industry to experiment extreme configurations and technological solutions. Examples of this are tilt-rotors (e.g., the Bell XV-15) or hybrid configurations with a rotor and one or two propellers (such as Sikorsky X2 or Airbus Helicopter X3), or adaptive rotors (such as the DARPA Mission Adaptive Rotor (MAR).

Potential approaches to reach this goal are variable blade diameter, sweep, chord, variable camber airfoils, varying blade twist, anhedral/dihedral, tip speed, stiffness, and damping. Some studies in the field have demonstrated the aerodynamic and acoustic benefits of an active twist rotor [3,41], rotor power reduction using trailing edge flaps or envelope expansion using extendable chord Sect. [4]. Probably, the most developed type of morphing in the field is related to twist, obtained with aeroelastic effects produced by trailing edge control surfaces and "smart spar," i.e., variable stiffness spar to create aeroelastic twisting.

Airfoil morphing is mainly concerned with camber variations: to a larger extent, the camber of an airfoil describes its asymmetry and is typically used to control its zero-lift angle of attack [10]. Adding camber, for example, will tend to increase the amount of lift produced at a given angle of attack of the airfoil, although this is limited by stall and separation. Almost all modern aircraft use discrete control surfaces, such as flaps, ailerons or sometimes slats, to adjust the camber of the wing. Trailing edge devices are control surfaces typically hinged at 75% of the chord which rotate to change their angle and also translate in some cases to increase

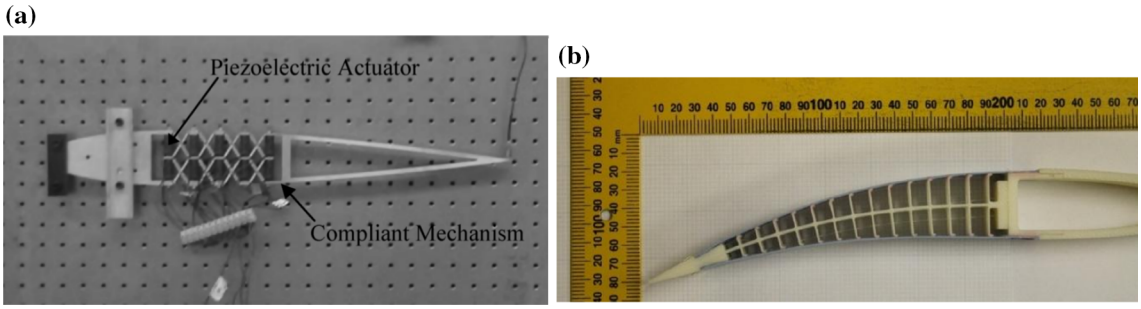

Fig. 2 Technologies for variable camber morphing: **a** prototype of conformable camber airfoil with piezoelectric actuators developed in Ref. [12], **b** FishBAC structure [30]

chord as well as camber. In helicopter rotor blades, trailing edge flaps have been extensively considered for vibration reduction over the last decades [12]. For instance, flaps are considered in the Boeing Smart Materials Actuated Rotor Technology (SMART) rotor project focused on the development of controllable rotors with smart-material actuators [19,35]. However, the camber change is almost always discrete in that after actuation of the control surface, there is a sudden transition of camber in the chordwise direction. This causes a sudden change in the pressure distribution over the corner created at the hinge line, causing a drag penalty and the possibility of separation. As a result, a smooth variation of camber obtained by airfoil morphing is an attractive solution to increase the lift coefficient in particular conditions of flight.

Variable camber airfoils have been adopted in fixed-wing applications [2,7], and this solution has recently been explored for helicopter applications, as well. To this extent, a continuously changing rotor blade airfoil is seen as a successor to rotor blade trailing edge flaps [12]. In Ref. [18], an adaptive airfoil with an aerodynamically smooth variable leading-edge droop is used to postpone dynamic stall. A variable camber airfoil based on a compliant mechanism and piezoelectric actuators is developed in Ref. [12] (see Fig. 2a). The morphing device is used for active helicopter vibration reduction. In this case, the shape of the airfoil is fixed, but an optimization is performed to find the optimal material distribution to maximize the trailing edge deflection under actuation forces and minimize the deflection under external aerodynamic loads. Another important study in the field is the development of the FishBone Active Camber (FishBAC) concept introduced and developed in Refs. [30–32]. The FishBAC is made of a compliant spine and stringer skeleton, pretensioned elastomeric matrix composite skin, an antagonistic tendon drive linked to a non-backdrivable spooling pulley, and a non-morphing,"rigid," main spar (see Fig. 2b).

Another solution in the literature is proposed in Ref. [24]. In this case, a variable droop leading edge is used to improve the sectional lift-to-drag ratio by alleviating dynamic stall on the retreating blade while simultaneously reducing the transonic drag rise of the advancing blade. A leading-edge variation combined with a trailing edge camber variation is the solution presented in Ref. [37] to define shock-free airfoils for helicopter rotors.

Because morphing structures typically imply increased weight, complexity and cost, an in-depth assessment of the potential aerodynamic benefit of such an approach is strongly recommended [30]. As a final remark, optimization of the morphing airfoil shape to improve the aerodynamic performance is typically run separately to the morphing mechanism design [10]. To this extent, the optimization approach is conceived as a two-level approach [7]: (i) the best deformed airfoil configuration is determined according to a desired aerodynamic performance, and (ii) in the second level, the best internal structural configuration is obtained using a topology optimization suited to the chosen compliant structure able to adapt itself in order to match the optimal shape coming out from the first level.

In this paper, we present a novel framework for obtaining optimal morphing airfoils under uncertain operating conditions. This is a quite novel approach in the literature, permitting to improve the overall performance of the system. Different types of geometry constraints are considered. The effect of camber and thickness morphing is discussed, and trailing edge morphing is studied. The gain of the morphing airfoil strategy is assessed not only from a deterministic point of view, but also when considering uncertainty in the operating conditions. In such a way, a more realistic estimate of the gain of morphing strategies can be defined.

In the following, Sect. 2 is devoted to the description of some numerical ingredients, which are used in this paper. Then, a discussion on two different choices of the morphing strategy is presented in Sect. 3 to assess the capability of morphing airfoils. In this first part, only deterministic evaluation is presented, because

deterministic optimal shapes (and corresponding operating conditions) represent the good starting point of robust approaches. This discussion demonstrates how camber morphing is more effective to enhance the aerodynamic performance. Then, optimal shapes from deterministic and robust approaches are computed and presented in Sect. 4. Finally, the validation over the azimuthal angle is presented in Sect. 5. Some conclusions and perspectives are then drawn in Sect. 6.

2 Numerical ingredients

The problem of defining optimal airfoil shapes can be cast in an optimization problem, which seeks to minimize an a priori defined objective function by acting on the shape of the airfoil.

The framework proposed in this paper requires many ingredients that need to be defined. Note that different choices are possible for each ingredient, even if all the methods used here are assumed to be highly performing with respect to the application of interest. To begin with, a parameterization is necessary to translate the airfoil shape into a finite set of sufficiently small design variables. Then, a method to estimate the cost function (e.g., drag or lift-to-drag ratio) for each combination of design variables must be chosen. For an aerodynamic optimization problem, this method is the solver of an aerodynamic model. Finally, an optimization algorithm is necessary to obtain the optimal solution.

2.1 Parameterization and design variables

The class/shape function transformation (CST) [20] is used to describe an airfoil shape with a finite set of variables. This technique is retained here since it has shown in the literature the capability to represent a wide variety of 2D geometries with a relatively few scalar parameters (for more details see for example [29]).

The parameterization is well defined by specifying two functions: a geometry class function C and a shape function S that defines the particular shape of the geometry. In this case, the airfoil shape is decomposed into the camber mean line and the normal thickness distribution. The thickness distribution is taken in perpendicular direction with respect to the camber mean line.

Then, the camber line and thickness distribution are such that the upper surface ζ_u and lower surface ζ_l are obtained applying the thickness perpendicular to the camber line, as follows:

$$\begin{aligned} \zeta_u &= \zeta_c + \zeta_t \cos(\epsilon), \\ \zeta_l &= \zeta_c - \zeta_t \cos(\epsilon) \end{aligned} \tag{1}$$

where $\epsilon = \arctan\left(\frac{\mathrm{d}\zeta_c}{\mathrm{d}\chi}\right)$. Please note that also the χ coordinate of the resulting airfoil will be affected by this addition of vectors.

Note that the coordinate of the camber mean line at the trailing edge is set to zero to consider closed trailing edge and zero geometric angle of attack. In addition, the class functions for the camber line C_c and the thickness distribution C_t are defined as follows:

$$C_c(\chi) = \chi(1-\chi), \quad C_t(\chi) = \sqrt{\chi}(1-\chi). \tag{2}$$

While the class function for the thickness distribution is the one suggested in Ref. [20] to define a rounded nose distribution close to the leading edge, the class function for the camber presents a linear term to avoid vertical slope of the camber distribution at the leading edge. In addition, the linear term of the class function permits to directly relate the first coefficient of the shape function A_0^c with the slope of the camber line at the leading edge. In addition, the linear term of the class function permits to directly relate the first coefficient of the shape function A_0^c with the slope of the camber line at the leading edge.

The shape function $S(\chi)$ is given by a Bernstein polynomial of order N, whose coefficients $\{A_i^c\}_{i=1}^N$ represent the design variables $\boldsymbol{x}_s$ of the optimization problem. A convergence study suggested the employment of fourth-order polynomials for each distribution that yields 10 design variables. The order of the polynomial could be chosen based on a convergence analysis of the CST (for further details, see Ref. [11]). Because the camber is built as the product of the class function and the shape function, the linear term in C_c permits to directly relate the coefficient of the shape function A_0^c (i.e., the constant term of the polynomial) with the slope of the camber line at the leading edge.

In addition to the coefficients describing the shape of the airfoil, the angle of attack can be regarded as a design variable. In fact, it is possible to solve the constrained optimization problem by acting on the airfoil design variables $\boldsymbol{x}_s$ to minimize the drag coefficient and on the angle of attack to track the target lift coefficient inside two nested loops. The underlying idea is an analogy with the blade collective pitch control: to increase thrust it is necessary to act on the collective pitch, which changes the angle of attack of the blade section through the alteration of the inflow angle.

Thus, each airfoil tested in the optimization loop is obtained with a specific set $\boldsymbol{x}_s$, and its performance is evaluated computing the angle of attack α that provides the desired lift coefficient. The nested optimization loops used to implement this procedure are described in detail in Sect. 2.3. Thus, the resulting set of design variables is $\boldsymbol{x} = \{\boldsymbol{x}_s, \alpha\}$.

2.2 Aerodynamic models

A model describing the aerodynamic load acting on the airfoil is necessary to compute the objective function of the optimization problem. The aerodynamic models used in this optimization problem are different for each side of the blade in order to capture the specific features of the flow in such different operating conditions, while limiting the computational effort.

In the retreating side featuring subsonic condition below the static stall boundary, the XFOIL code [8] is adopted, which is an aerodynamic code with coupled panel and integral boundary layer methods developed for the analysis of subsonic, isolated airfoils [8]. This code is chosen because it provides a fast and sufficiently accurate estimation of the aerodynamic force coefficients for a two-dimensional section in the range of angle of attack considered in this problem. Please note that the highest value of the angle of attack in the range is below the static stall limit for most airfoils. Note also that although dynamic stall has significant impact on forward flight rotor performances, its effects are not included in the design of an airfoil at this stage mainly for two reasons: (i) the capability to simulate correctly the loads developed during a dynamic stall is limited even by using numerically demanding models, and (ii) the dynamic stall is strongly influenced by three-dimensional effects [40].

For fully developed transonic conditions, like the one experienced in forward flight, a finite volume-based numerical solver of the Euler equations is used, the Stanford University Unstructured (SU^2) software suite [33,34]. The SU^2 solver provides several space discretization schemes, among which the second-order Jameson–Schmidt–Turkel scheme is employed. An implicit Euler, local time-stepping is used to converge to the steady-state solution, and the GMRES method in conjunction with the LU SGS preconditioner is used to solve the resulting system [13].

For the computation inside the optimization loop, a two-dimensional coarse structured mesh of 20,480 rectangular cells is used, with $y+ = 1000$ (see Fig. 3). The mesh extends ± 25 chords around the unitary-chord airfoil. For each airfoil in the optimization loop, the computation runs for 500 iterations starting from a baseline solution of the NACA0012 airfoil. This number of iterations is used to ensure that the solution reaches a variation of the lift and drag coefficients lower than 10^{-6}. The mesh is deformed by displacing the airfoil boundary cells according to the new geometry and by translating the displacement to the volume cells with a method based on the finite element method discretization of the linear elasticity equations [33]. The element stiffness is set inversely proportional to the wall distance, and 500 smoothing iterations are applied to get a regularly deformed mesh. Concerning the boundary conditions, wall and far-field characteristic-based conditions implemented in SU^2 have been considered. The total cost of a single CFD iteration is about 400 s on a single core.

2.3 Optimization algorithm

In the following sections, different optimization problems will be solved. A general formulation for them is the following:

$$\begin{aligned} &\text{minimize: } \mathbf{f}(\boldsymbol{x}) \\ &\text{subject to: } \mathbf{g} <= 0 \\ &\text{by changing: } \boldsymbol{x} \end{aligned} \tag{3}$$

where $\mathbf{f}$ is a vector of objective functions which depends on the airfoil lift and/or drag coefficients, and $\boldsymbol{x}$ are the design variables (described in Sect. 2.1). The objective function vector $\mathbf{f}$ contains a single element in the

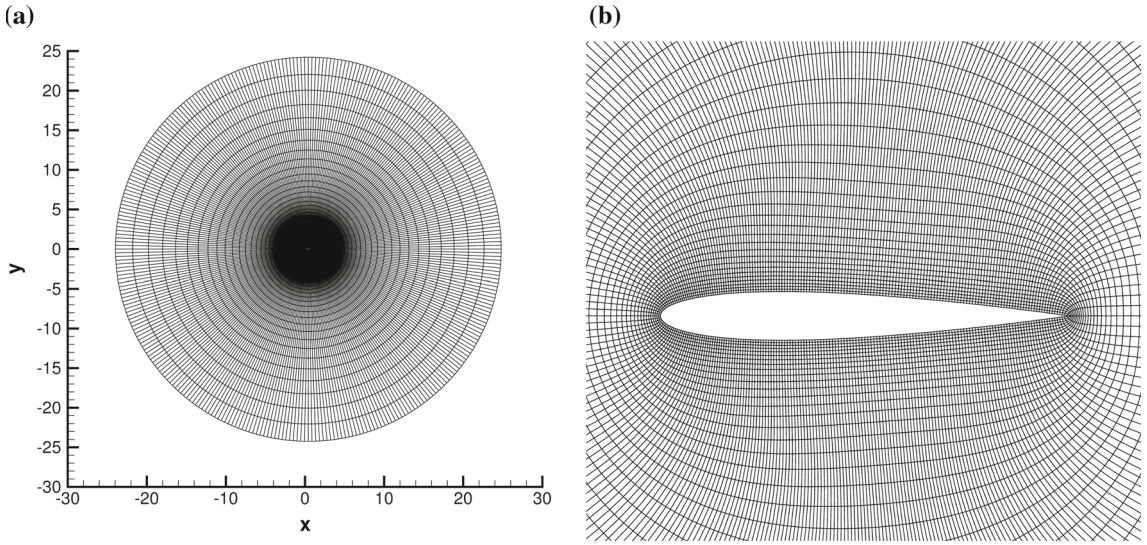

Fig. 3 Coarse structured grid (20480 cells) for Euler computations inside the optimization loop. **a** O-mesh; **b** zoom

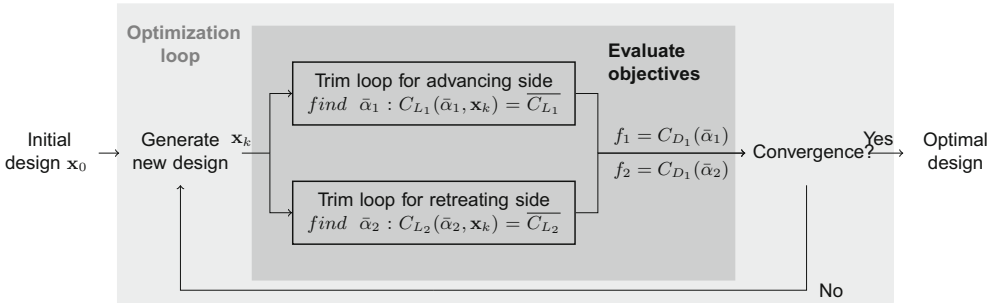

Fig. 4 Outer NSGA loop for $\boldsymbol{x}_s$ and inner trim loop to determine $\overline{\alpha}$

case of a single-objective optimization, or more in case of multi-objective functions. Equality and inequality constraints **g** are present: for instance, a lift equality constraint is used to ensure the airfoil produces the sufficient amount of lift that ensures trim to the rotor, or an inequality constraint for the moment coefficient, to limit the load on the blade.

To solve the optimization problem, a Non-dominated Sorting Genetic Algorithm [36] is chosen for its ability to explore the design space.

Evolutionary algorithms have been employed to tackle many engineering optimization problems. Applications to aerodynamic optimization problems can be found for instance in Refs. [6,21,23]. Main advantages of such approaches are the possibility to tackle multi-objective problems without scalarization and to exhaustively explore the design space. On the other hand, they are very expensive from a computational point of view because they require many computations of the objective function, even in a region of the domain where designs with poorer performance are present. Genetic algorithms use operators inspired by natural evolution to get to the optimal solution. In such a framework, each design vector is considered as an individual, and the design variables in the vector represent the chromosomes. A group of individuals is called a generation. Each individual is assigned a fitness function, that is a measure of the probability that this individual will be a parent of the individuals of the next generation. The fitness in the optimization algorithms is associated with the objective function: the better the objective function, the higher the fitness value. In the single-objective case, the fitness function is a measure of the objective function. In the multi-objective case, the fitness function is assigned based on the position of the individual in the objective space with respect to the current Pareto front. With the fitness value, the selection step is performed to determine the parents of the new generation; mutation and crossover operators are then used to maintain genetic diversity and to obtain different children from a single set of parents. The genetic algorithm performs a loop over the generations. The starting point is an initial generation of individuals that are typically randomly chosen. For each iteration, a new generation of

individuals is computed using selection, crossover, and mutation operators. Then, the objective functions are evaluated for each individual, and each design vector is assigned a fitness function. From the fitness of these individuals, a new generation is computed, and the loop goes on for a sufficient number of generations.

Typical values for the crossover and mutation probabilities pc $= 0.9$, pm $= 0.1$ are chosen, and the sharing parameter is set using a formula based on the number of design variables.

Because of the presence of the lift coefficient equality constraint, which can be satisfied with a separate design variable (the angle of attack), an inner loop is nested inside the genetic algorithm loop (see Fig. 4). In particular, for each design vector $\boldsymbol{x}_{s,k}$ of the kth iteration in the genetic loop, a secant method is used to find the angle of attack $\overline{\alpha}$ that guarantees $C_{L,k} = \overline{C_L}$. The ith iteration of the secant loop reads

$$\alpha_i = \alpha_{l_i} + \frac{\alpha_{r_i} - \alpha_{l_i}}{C_L(\alpha_{r_i}) - C_L(\alpha_{l_i})} \left(\overline{C_L} - C_L(\alpha_{l_i})\right) \tag{4}$$

where α_{l_i} and α_{r_i} are the left and right boundaries of the interval in which the angle of attack is sought, and they satisfy: $C_L(\alpha_{r_i}) > \overline{C_L}$ and $C_L(\alpha_{l_i}) < \overline{C_L}$. The left and right values are updated according to the value of the lift coefficient for the current α_i: if $C_L(\alpha_i) > \overline{C_L}$, then $\alpha_{r_{i+1}} = \alpha_i$; if $C_L(\alpha_i) < \overline{C_L}$, $\alpha_{l_{i+1}} = \alpha_i$, and if $\overline{C_L} - \varepsilon \leq C_L(\alpha_i) \leq \overline{C_L} + \varepsilon$, with a tolerance $\varepsilon = 10^{-3}$, the loop breaks.

The method converges in a few iterations, owing to the quasi-linearity of the lift coefficient for most airfoils in the vicinity of the considered values of the angle of attack. Lack of convergence within few iterations may happen in the retreating side (i.e., for high values of the angle of attack) for airfoils close to stall conditions that will be discarded in the optimization process because they will have a poor drag coefficient. The result of the two nested loops is a set of optimal solutions defined by a design vector $\{\boldsymbol{x}_s, \alpha\}$.

Because we are using a genetic algorithm, the error on the lift coefficient constraint for those airfoils should not affect the optimization process.

It is noted that the inner trim loop targets the equality constraint on the lift coefficient, but the design vector coming out of it may not satisfy the moment coefficient constraint.

3 Effects of camber and thickness morphing

In this section, the effect of modification of the thickness and the camber of the airfoils is discussed. An airfoil geometry can be characterized by the coordinates of the upper and lower surface. However, an airfoil can also be described by the construction of a thickness shape distributed around a camber line. This description dates back to the 1920s and 1930s, when the NACA 4-digit and 5-digit airfoils were generated by superimposing a simple meanline shape with a thickness distribution that was obtained by fitting a group of popular airfoils of the time.

The camber mean line mainly affects the chordwise load distribution, the angle of zero lift, the pitching-moment coefficient, the slope of the lift curve, and the approximate position of the aerodynamic center [1, p. 65]. Effects of increasing the camber line are generally a lower zero-lift angle of attack and a higher maximum lift coefficient. The counterpart of this is an increase in the drag coefficient, especially at low angle of attack, and an increase in the pitching-moment coefficient. This latter problem, which is crucial in helicopter blade design, led to the almost universal use of symmetric airfoil sections on helicopters developed before the 1960s [22, p. 360]. However, with the advent of new camber line distribution, such as the NACA 23012 airfoil which is designed to limit the moment coefficient, cambered airfoils were introduced also in rotorcraft blades. A clear example of the effect of camber on the moment coefficient is given by reflexed airfoils, which have reduced camber over the afterward section producing less lift over this region, thereby less nose-down pitching moment. In this case, the aft section is actually generating downforce, and the moment coefficient at zero lift is positive.

Effects of the thickness distribution include the increase in the maximum lift coefficient with increasing thickness, at least for thickness-to-chord ratio in the range used for aeronautical applications (i.e., around 16% [1, p. 135] for the NACA 4- and 5-digit airfoils), above which the effect of thickness become detrimental for separation. Thickness distribution has a significant impact on profile drag and on wave drag. With regard to the latter, earlier drag rise and lift break are experienced for a thicker airfoil [1, p. 274], although this is in general an effect of both thickness-to-chord ratio and distribution and may vary from airfoil to airfoil.

Table 1 Aerodynamic coefficients of NACA 23012 airfoil

Case	α (°)	M (–)	Re (–)	C_L (–)	C_D (counts)	C_M (–)
1.	− 1.5	0.75	4.6e6	− 0.025	86.97	0.02
2.	12.5	0.28	1.7e6	1.411	191.3	0.03

Table 2 Operating conditions and aerodynamic constraints

Case	M (–)	Re (–)	$\overline{C_L}$	$\overline{C_M}$	w_i (1/counts)
1.	0.75	4.6e6	0.025	0.08	1/2
2.	0.28	1.7e6	1.411	0.04	1/160

3.1 Camber and thickness morphing from an optimal trade-off airfoil

In this section, an ideal morphing strategy is investigated: the assumption is that the morphing mechanism permits to have no geometry constraints to the airfoil shape between the advancing and retreating side, and then, each shape is designed by running a shape optimization in one specific operating condition. The interest is to compute an ideal reference gain, with a morphing strategy that could morph the section of a blade from the optimal shape in the advancing side to the optimal shape in the retreating side.

3.1.1 Deterministic optimization

Then, a deterministic optimization of a helicopter rotor airfoil in forward flight is performed, which consists typically in the minimization of the drag coefficient C_D ensuring the satisfaction of constraints on the lift C_L and moment C_M coefficients [9,27,28]. The drag coefficient is used instead of torque, because a single radial station is considered, and a single airfoil is optimized. A complete blade optimization would need to minimize torque, by considering many airfoils in the spanwise directions and other design variables such as radial twist and chord.

Here, a target lift coefficient $\overline{C_L}$ is set to consider a specific trim condition, and the moment coefficient is bounded with a given threshold $\overline{C_M}$ to avoid excessive loading on the blade structure. The objectives of the advancing and retreating side are conflicting with one another. In fact, an optimal shape for the advancing side would be a mildly cambered airfoil to postpone drag rise to higher Mach number values, whereas the adoption of a highly cambered airfoil in the retreating side could better adapt to a higher angle of attack, for instance by means of a nose droop.

In mathematical terms, two single-objective optimization problems may be formulated as follows

$$\begin{aligned} &\text{minimize: } C_{D_i}(\boldsymbol{x}) \\ &\text{subject to: } C_{L_i}(\boldsymbol{x}) = \overline{C_{L_i}} \quad |C_{M_i}(\boldsymbol{x})| \leq \overline{C_{M_i}} \end{aligned} \tag{5}$$

where $\boldsymbol{x}$ are the design variables. The subscript i is equal to 1 in the advancing side and 2 in the retreating side. The blade section of the Bo105 rotor [38] at $r = 0.85$ is considered, and the operating conditions for advancing and retreating sides are taken from the corresponding "figure-of-eight" in the (M, α)-plane from Ref. [16, p. 296]. Both operating Mach number and the corresponding constraints are reported in Table 2. The values of the lift constraint $\overline{C_{L_i}}$ are set for each side with the intent of producing a design that improves the performance of the NACA 23012 airfoil, a classical shape for helicopter rotors (the aerodynamic coefficients of the NACA 23012 airfoil in the operating conditions are presented in Table 1).

To complete the scenario of deterministic optimization problems, a one-objective optimization with a trade-off performance is performed. The optimization problems in this case is defined as follows:

$$\begin{aligned} &\text{minimize: } \frac{1}{2}\sum_{i=1}^{2} w_i C_{D_i}(\boldsymbol{x}) \\ &\text{subject to: } C_{L_i}(\boldsymbol{x}) = \overline{C_{L_i}} \quad |C_{M_i}(\boldsymbol{x})| \leq \overline{C_{M_i}} \;\; i = 1, 2 \\ &\text{by changing: } \boldsymbol{x} \end{aligned} \tag{6}$$

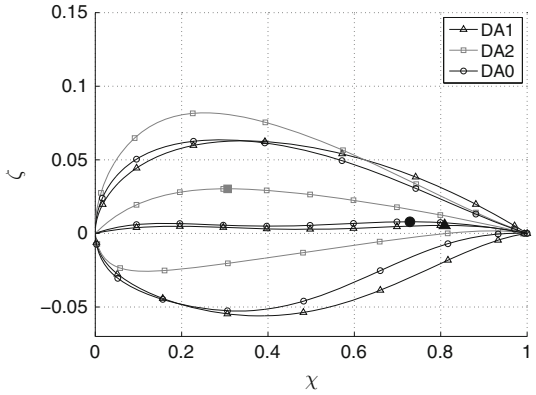

Fig. 5 Optimal airfoils (DA1, DA2, and DA0) for the different optimization problems

Table 3 Characteristics of the optimal airfoils (for unitary chord)

	DA1	DA2	DA0
Maximum thickness	0.1187	0.1049	0.1161
Position of maximum thickness	0.36	0.22	0.31
Maximum camber	0.0054	0.0303	0.0079
Position of max camber	0.81	0.31	0.73
First design variable (A_0^c)	0.065	0.289	0.107
Camber slope at LE (°)	3.704	16.098	6.108

Table 4 Performance of the optimal airfoils: performance of DA1 in the retreating side is not reported because DA1 airfoil cannot satisfy lift constraint

	C_{D_1} (counts)	$\alpha_1\|_{\overline{C_{L_1}}}$ (°)	C_{M_1} (–)	C_{D_2} (counts)	$\alpha_2\|_{\overline{C_{L_2}}}$ (°)	C_{M_1} (–)
DA0	0.8947	− 1.059	0.0463	177.8	11.1	− 0.0108
DA1	0.6927	− 1.002	0.0459	–	–	–
DA2	191.99	− 3.101	0.1047	126.0	9.27	− 0.0393

where w_i are weights chosen from the drag coefficient of the optimal airfoils obtained in the one-point optimization case (see Table 2). The result of such an optimization is a compromise solution between advancing and retreating side that is used as a reference of a trade-off optimal solution.

Then, three different deterministic optimization problems are solved, thus computing three optimal designs: (i) airfoil DA1 with optimal drag coefficient in the advancing side, (ii) airfoil DA2 with optimal drag coefficient in the retreating side, and (iii) airfoil DA0 with optimal weighted drag coefficients. These airfoils are presented in Fig. 5, and the characteristics of their geometry are reported in Table 3. Note that the optimal airfoil for the retreating side is highly cambered to cope with the higher angle of attack, and it has a lower thickness-to-chord ratio to reduce the drag coefficient. The optimal airfoil of the advancing side generates positive lift owing to a slight camber and greater thickness. The slope of the camber line at the leading edge is controlled by the first coefficient of the parameterization thanks to the modification of the CST discussed in Sect. 2.1.

The drag coefficients of the optimal airfoils are presented in Table 4. The drag coefficients are expressed in drag counts, where one drag count is equal to 0.0001. The gain with respect to the reference NACA 23012 airfoil is presented in Table 5. The DA1 airfoil and the DA2 airfoil significantly improve the performance of the advancing and retreating side, respectively.

3.1.2 Assessment in terms of morphing strategy

The optimized airfoils are presented in Fig. 6 in the space of the objectives of the deterministic optimization (i.e., the drag coefficient in the advancing and retreating side). Airfoil DA0 represents the reference optimal solution for a non-morphing configuration. Instead, airfoils DA1 and DA2 give an indication of the best possible

Table 5 Gain of the optimal airfoils with respect to the NACA 23012 airfoil: gain of DA1 in the retreating side and gain of DA2 in the advancing side are not reported because these airfoils do not satisfy, respectively, the lift and moment constraint

	Percentage gain side 1	Percentage gain side 2	Relative gain side 1	Relative gain side 2
DA0	+99%	+7 %	1/97.2	1/1.08
DA1	+99%	–	1/125	–
DA2	–	+34%	–	1/1.52

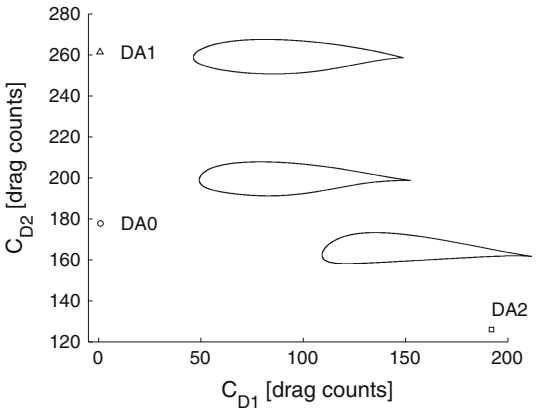

Fig. 6 Optimal deterministic shapes and drag coefficient in the advancing and retreating sides

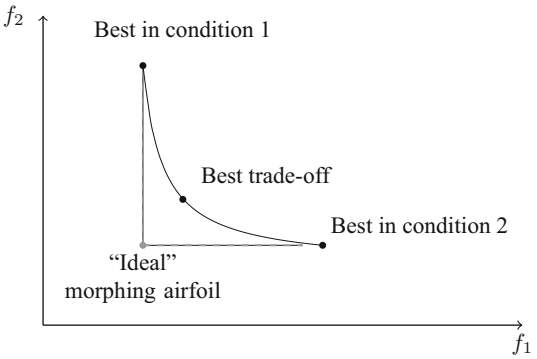

Fig. 7 Scheme of two-point optimization and "ideal" morphing airfoil

gain of a morphing strategy. In fact, the maximum, "ideal" gain of morphing airfoils consists of the gain of a morphing strategy that could morph the section of a blade from the shape of airfoil DA1 in the advancing side to the shape of airfoil DA2 in the retreating side. This is depicted in Fig. 7. This solution would have the lowest drag coefficient in the advancing side and at the same time the lowest drag coefficient on the retreating side. The morphing strategy is ideal in this case, because in practice any morphing mechanism would impose geometry constraints to the airfoil shape between the advancing side and retreating side that are not considered in this first instance. Indeed, state-of-the-art technology permits only local deformation of the camber line, as presented in the introduction, although an active field of research on materials is developing ways of increasing the degree of freedom of morphing geometries that could be adopted in future research activities. Nevertheless, the ideal gain is of the highest significance, because it sets a reference gain. The gain is computed with respect to the optimal non-morphing geometry, which in this case is the trade-off airfoil DA0. As presented in Table 6, such a "perfectly" morphing airfoil could gain 22% of the drag coefficient in the advancing side and 29% in the retreating side, while maintaining the trim lift coefficient and moment constraint.

To further support the choice of camber line morph over thickness distribution morph, a comparison is made among airfoils generated from airfoil DA0 imposing either the thickness distribution of airfoil DA1 or DA2 or the camber line. In other words, four airfoils are constructed by fixing either the thickness or the

Table 6 Gain of an "ideal" morphing with respect to the trade-off non-morphing solution DA0

	DA1 (%)	DA2 (%)
Gain w.r.t DA0	22	29

Table 7 Summary of airfoils obtained by imposition of either the thickness or camber line of DA1 and DA2 from DA0

	Thickness	Camber
Thick DA0 + Camb DA1	DA0	DA1
Thick DA0 + Camb DA2	DA0	DA2
Thick DA1 + Camb DA0	DA1	DA0
Thick DA2 + Camb DA0	DA2	DA0

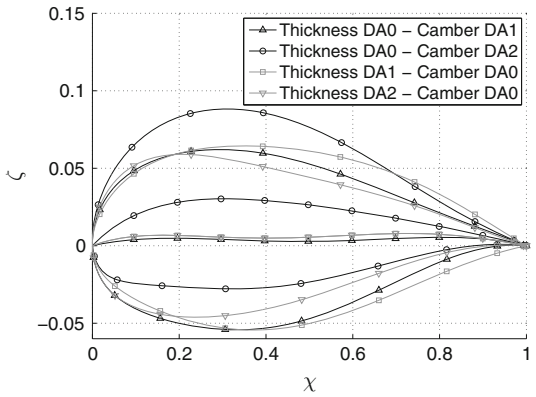

Fig. 8 Airfoils obtained by changing either the thickness or camber line from airfoil DA0

Table 8 Drag coefficient of airfoils obtained from deterministic optimal airfoils (see Table 7)

	C_{D_1} (counts)	$\alpha_1\|_{\overline{C_{L_1}}}$ (°)	C_{D_2} (counts)	$\alpha_2\|_{\overline{C_{L_2}}}$ (°)	Gain side 1	Gain side 2
DA0	0.8947	-1.059	177.8	11.1		
Thick DA0 + Cam DA1	0.805	-0.945	192.3	11.502	+10%	
Thick DA0 + Cam DA2	151.53	-3.316	141.6	9.55		+20%
Thick DA1 + Cam DA0	0.801	-1.128	–	–	+10.5%	
Thick DA2 + Cam DA0	11.26	-1.028	166.0	10.881		+6%

camber line of airfoil DA0 and imposing the camber line or the thickness of airfoils DA1 and DA2. The airfoils are summarized in Table 7, and the resulting shapes are presented in Fig. 8. The first two solutions refer to a camber morphing in which the camber is modified and the thickness is held constant (and equal to the one of the best non-morphing solution). On the other hand, the last two solutions represent a thickness morphing, where the camber is held fixed to the one of airfoil DA0.

For these airfoils, the angle of attack for which the lift coefficient satisfies the trim constraint (i.e., the constraint to produce the target lift coefficient) is computed, and the corresponding drag coefficients are evaluated. Results are presented in Table 8. As explained in Sect. 2.2, the Euler equations-based CFD model is used in the advancing side and XFOIL in the retreating side (see Sect. 2.2). Note that the solutions obtained by holding the thickness fixed and changing the camber line (Thick DA0 + Cam DA1 and Thick DA0 + Cam DA2) improve the gain of the reference DA0 airfoil by 10% in the advancing side and 20% in the retreating side. With respect to the ideal gains presented in Table 6, this solution restores 50% of the ideal gain in the advancing side and 90% in the retreating side. On the other hand, solutions obtained by modifying the thickness distribution present a similar gain on the advancing side (10.5%), but a smaller gain in the retreating side (6%). These results show that the camber morphing gets closer to the ideal morphing gain, and it is therefore more effective. Furthermore, it seems that the thickness and camber line equally contribute to the ideal gain in

Table 9 Performance of Thick DA0 + Cam DA2 airfoil in both sides

$\alpha_1\|_{\overline{C_{L_1}}}$ (deg)	$C_{D_1}\|_{\overline{C_{L_1}}}$ (counts)	$C_{M_1}\|_{\overline{C_{L_1}}}$	$\alpha_2\|_{\overline{C_{L_2}}}$ (°)	$C_{D_2}\|_{\overline{C_{L_2}}}$ (counts)	$C_{M_2}\|_{\overline{C_{L_2}}}$
−3.316	151.53	0.109153	9.55	0.01416	−0.0414

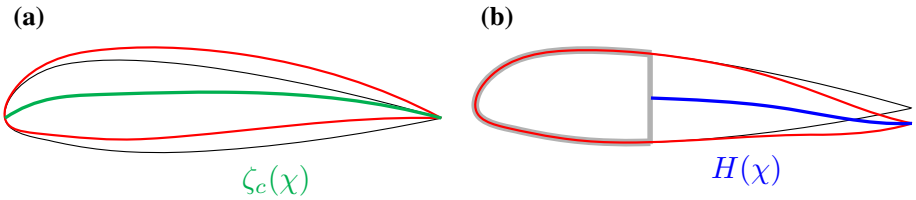

Fig. 9 Types of morphing strategy: baseline geometry (black), camber morph (green) or trailing edge morph (blue) and resulting morphed geometry (red): **a** camber line morphing, **b** trailing edge morphing (color figure online)

the advancing side, while in the retreating side the camber line plays a key role. As a matter of fact, in the advancing side transonic flow is experienced, and the minimization of the drag coefficient corresponds to the minimization of wave drag. This contribution equally depends on camber and thickness distributions over the chordline. On the other hand, high angle of attack and subsonic flow are encountered in the retreating side; thus, the gain is basically built upon the adaptation of the airfoil to the high angle of attack achieved by camber.

Finally, results for airfoil Thick DA1+Cam DA0 in the retreating side are not presented because this airfoil cannot meet the trim constrained, as it happened with airfoil DA1 (see Table 4). In a similar way, an airfoil with DA0 thickness and DA2 camber exceeds the moment coefficient in the advancing side as presented in Table 9 (similarly to what happened for DA2, please refer to Table 4). To some extent, these airfoils obtained by a combination of thickness and camber of DA0, DA1, and DA2 inherit some of the characteristics of the original airfoils. However, it is noted that the moment coefficient of the airfoil Thick DA1+Cam DA2 also exceeds the threshold value $\overline{C_{M_2}}$ set in the optimization loop (see Table 9).

4 Optimal morphing airfoils

The optimization problems tackled in the case of morphing airfoils maintain the same structure as the cases presented in Sect. 3.1.1. Thus, two optimization problems are performed, one for the advancing side and one for the retreating side, which seeks the design with minimal drag coefficient with an equality constraint on the lift coefficient and an inequality constraint on the moment coefficient. The same values of target lift coefficients, bounding moment coefficients, and operating conditions are used (please refer to Table 2).

The difference in this case is that the optimization is performed by acting on the design variables describing the morphing geometry. The morphing design variables are described in the following section.

4.1 Morphing strategy and parameterization

The morphing strategy considered in this work is a conformable camber airfoil, which changes over the period of rotation of the blade. Several technological solutions can be employed to achieve this goal: for instance, the FishBone Active Camber [30], the controllable camber presented in Ref. [12], and chiral structures as the one developed in Ref. [2]. The basic idea in the definition of a camber morphing airfoil is that the thickness distribution is held fixed, while the camber is allowed to change its shape during flight.

The type of morphing introduced to some extent in the previous section permits modification of the camber over the entire chordwise coordinate. However, in general the camber line cannot be modified at any chordwise coordinate, but it is held fixed in particular areas to maintain the internal structure of the blade and to accommodate morphing mechanisms. In general, the region close to the leading edge is fixed, where the *D*-shaped spar used in the helicopter blade structure is found. Thus, two types of camber morphing are considered. In the first case (Fig. 9a), complete freedom is given to the camber line. In the second type (Fig. 9b), the first part of the airfoil is fixed, while for the remaining part of the blade section the camber can morph

Table 10 Summary of optimization problems

Case	Objective	Equality constraints	Inequality constraints	Design variables
DMO1	$\min C_{D,1}$	$C_{L_1} = \overline{C_{L_1}}$	$\lvert C_{M_1}\rvert \leq \overline{C_{M_2}}$	$\boldsymbol{x}_{m,c}, \alpha$
DMO2	$\min C_{D,2}$	$C_{L_2} = \overline{C_{L_2}}$	$\lvert C_{M_2}\rvert \leq \overline{C_{M_2}}$	$\boldsymbol{x}_{m,c}, \alpha$
DTO1	$\min C_{D,1}$	$C_{L_1} = \overline{C_{L_1}}$	$\lvert C_{M_1}\rvert \leq \overline{C_{M_2}}$	$\boldsymbol{x}_{m,te}, \alpha$
DTO2	$\min C_{D,2}$	$C_{L_2} = \overline{C_{L_2}}$	$\lvert C_{M_2}\rvert \leq \overline{C_{M_2}}$	$\boldsymbol{x}_{m,te}, \alpha$

Table 11 Performance of the deterministic airfoils obtained with two strategies for camber morphing

Morphing	Objective	C_{D_1} (counts)	$\alpha_1\lvert_{\overline{C_{L_1}}}$ (°)	C_{D_2} (counts)	$\alpha_2\lvert_{\overline{C_{L_2}}}$ (°)	Gain side 1	Gain side 2
Camber	$\min f_1$	0.805	−0.945	192.3	11.502	+10%	
Camber	$\min f_2$	102.82	−2.5	135.7	9.62		+23%
TE morph	$\min f_1$	0.8947	−1.059	177.8	11.1	0%	
TE morph	$\min f_2$	100.50	−1.93	169.2	10.045		+5%

and work as a trailing edge flap with a larger extension and continuous shape modification. In this way, an increasing level of constraints to the morphing strategy is given: (i) ideal morphing, with constraints neither on the thickness nor on the camber line, (ii) camber morphing, with a fixed thickness distribution, and (iii) trailing edge morphing, with a fixed thickness distribution and a partial constraint on the camber line.

A suited parameterization is required to describe and optimize a morphing camber airfoil. The parameterization introduced in Sect. 2.1 treats separately the camber line and the thickness distribution perpendicular to the local camber line. For the entire camber morphing, the design variables are the coefficients A_i^c of the shape function $S_c(\chi)$ used to describe the camber distribution as $\zeta_c(\chi) = C_c(\chi)S_c(\chi)$. The class function is the same function as that presented in Eq. (2). The order of the Bernstein polynomials is retained from the optimization in forward flight condition, but owing to the fact that the thickness distribution is now fixed, the number of design variables is reduced by half. It follows that the design variables for the case of camber morphing are $\boldsymbol{x}_{m,c} = \{A_i^c\},\ i = 0, \ldots, 4$.

For the trailing edge morphing modification, a piecewise cubic function is used. The cubic functions are defined to ensure continuity up to the second order. Following an approach similar to the one presented in Ref. [10], the morphing camber line is described as follows:

$$\begin{aligned} \zeta_c(\chi) &= C_c(\chi)\, S_c(\chi) + H(\chi), \\ H(\chi) &= \sum_{i=1}^{n_c} h_i(\chi), \end{aligned} \tag{7}$$

and each cubic function $h_i(\chi)$ reads

$$h_i(\chi) = \begin{cases} 0, & \text{if } \chi \leq \psi_{0,i} \\ A_i^m \frac{(x-x_{0,i})^3}{(1-x_{0,i})^3}, & \text{if } \chi > \chi_{0,i} \end{cases}$$

where A_i^m are the coefficients of the cubic functions, and $x_{0,i}$ are the locations of the start of the morph. The number of cubic functions n_c is equal to two in order to represent also reflex cambered airfoil, and the locations of the morphs are $x_{0,1} = 0.4$ and $x_{0,2} = 0.7$. The D-spar length $x_{0,1}$ is set to 40% of the chord, following the FishBAC configuration [10]. The coefficients of the cubic functions are the design variables of the morphing airfoil $\boldsymbol{x}_{m,te} = \{A_1^m, A_2^m\}$.

4.2 Deterministic results

With two different operating conditions and two different morphing strategies, four optimization problems are performed, which are summarized in Table 10. Each optimization has been performed with an initial generation

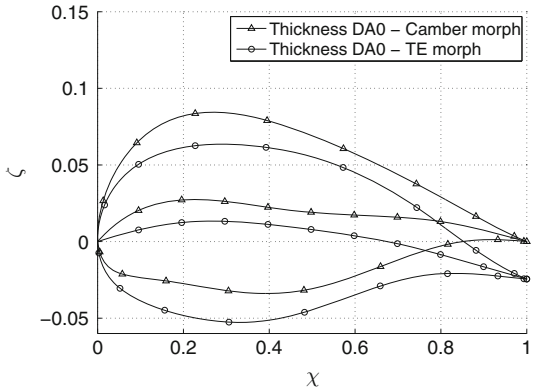

Fig. 10 Airfoils obtained by morphing the camber mean line of airfoil DA0

of 100 individuals and 10 generations of 55 individuals to widely explore the solution space. The results of these optimizations are reported in Table 11, where the first and second columns indicate the morphing strategy and the objective, respectively. The last two columns present the gain with respect to the optimal non-morphing airfoil, i.e., airfoil DA0.

The camber morphing involving the entire camber line permits to gain 23% with respect to DA0 in the retreating side and 10% in the advancing side. In the latter condition, the optimal solution obtained by the optimization is indeed the airfoil obtained by summing the thickness distribution of DA0 to the camber line of airfoil DA1, i.e., Thick DA0+Cam DA1. In the retreating side, the optimization is capable of improving the drag coefficient of airfoil Thick DA0+Cam DA2 and at the same time overcoming the problem associated with the moment coefficient constraint.

On the other hand, the trailing edge morphing improves the starting airfoil by 5% in the retreating side, but it does not find better solutions than airfoil DA0 in the advancing side. A first explanation of this can be found in the fact that airfoil DA0 has a shape more akin to DA1 than DA2 (see Fig. 6), and it is an airfoil that already significantly reduces the wave drag coefficient of the reference airfoil (i.e., the NACA 23012 airfoil shown in Table 1). However, the modification that the camber needs to undergo to improve the performance in the advancing side (for example, a modification into the camber line of airfoil DA1) is not compatible with the trailing edge modification shown in Fig. 9b. This problem could be overcome only by changing the thickness distribution together with the trailing edge modification. The best gain of such a strategy may be defined only by an optimization problem combining the coefficient of the thickness distribution A_i^t, the coefficient of the mean line A_i^c, and the coefficient of the local trailing edge morph A_i^m.

To appreciate the difference in the morphing strategies, the optimal airfoils for the retreating side are presented in Fig. 10. It is worth noting how the camber morphing lifts up the camber line while maintaining the trailing edge location, and the trailing edge morph deflects the trailing edge to achieve an increase in the lift coefficient.

4.3 Results under uncertainty

From the deterministic optimization, valuable information has been obtained. In fact, the camber morphing could potentially bridge the gap between a non-morphing airfoil and an "ideal" morphing airfoil, and the morphing over the entire chordwise distribution of the camber line is more effective to this purpose. Starting from these results, the robust optimization problems are tackled in this section. Note that the design variables used in this case are the design variable of the camber morphing $\boldsymbol{x}_{m,c}$, as this technique is more effective.

The objective of robust optimization is to design an airfoil that is minimally sensitive to the variation of the operating conditions. In this case, it is considered that the operating conditions at which the blade section will operate are affected by the uncertainty arising due to modeling assumptions of physical parameters necessary at the design stage.

4.3.1 Robust optimization formulation

Due to the uncertainty, the objective function f is no longer only a function of the design variables $\boldsymbol{x}_{m,c}$, but it also depends on the uncertain variables $\boldsymbol{\xi}$. Within this uncertain framework, a minimization with a target lift coefficient in a specific design condition loses its meaning. However, a robustly optimal airfoil with a satisfactory lift-to-drag ratio in a range of conditions could be used to trim the aircraft in a specific condition keeping always a low drag coefficient. In addition, if the robustness of the lift-to-drag ratio will translate into the drag coefficient at a specific target lift coefficient, a robust shape would ensure less variability of the required power due to aerodynamic drag.

In particular, for the problem under analysis, the following objectives are defined for each side of the blade.

1. On the advancing side, rotor blade encounters transonic flow, so airfoils should typically be designed to delay drag divergence to higher Mach numbers [5,22]: however, since the airfoil should feature also a certain amount of lift, the lift-to-drag ratio is maximized for the first condition corresponding to the advancing blade at 90°, with the constraint of providing a lift coefficient equal to or larger than the value of the reference NACA 23012 airfoil. Thus, the lift-to-drag ratio C_L/C_D is the objective f_1 of the optimization: $f_1 = C_L/C_D$.
2. On the retreating side, the increase in the lift coefficient is typically sought [5]: however, to account for drag reduction as well, for the blade at 270° the ratio $C_L^{3/2}/C_D$ is maximized, which is a measure related to the rotor figure of merit in hover [22] that privileges the lift coefficient over the drag coefficient, i.e., $f_2 = C_L^{3/2}/C_D$.

The nominal operating conditions of the aerodynamic simulation are set using data from Ref. [16]. Finally, the constraints on the moment coefficient used in the deterministic case (and presented in Table 2) are still considered.

In mathematical terms, the resulting optimization problem can be stated as:

$$\begin{aligned} \text{maximize:} \quad & \mu\left(f_i\left(\boldsymbol{x}_s, \boldsymbol{\xi}\right)\right) \\ \text{and minimize:} \quad & \sigma^2\left(f_i\left(\boldsymbol{x}_s, \boldsymbol{\xi}\right)\right) \\ \text{subject to:} \quad & \mathbf{g}\left(\boldsymbol{x}_s, \boldsymbol{\xi}\right) \leq \mathbf{0} \\ \text{by changing:} \quad & \boldsymbol{x}_s \end{aligned} \tag{8}$$

where the moment constraints are collected in vector $\mathbf{g}$. Similarly to the deterministic case, function f_i is equal to f_1 for the advancing side and equal to f_2 in the retreating case. The design variables are the variables defining the shape of the airfoil, while the angle of attack is considered as one of the uncertain variables in the robust design problem.

Indeed, the angle of attack α and the Mach number M encountered by the two-dimensional section of the blade are considered as uncertain, because they are affected by uncertainty on the modeling of the physical parameters considered in the design stage. For instance, both aerodynamic and structural uncertainties, such as blade chord, air density and rotor angular velocity, may affect the value of the angle of attack and Mach number. Following a probabilistic framework, the uncertain variables are modeled as uniformly distributed random variables around a nominal value. The nominal conditions are reported in Table 1, and the uncertainty band is set to 5% for the Mach number and for the angle of attack.

The objective functions of Eq. (8) are the statistics of the performance f. These are computed by means of an uncertainty propagation technique, that is a method to propagate the uncertainty affecting the operating conditions into the quantity of interest f.

4.3.2 Uncertainty quantification technique

A probabilistic framework is employed to deal with the uncertain input data. In this context, the stochastic input quantities $\boldsymbol{\xi}$ are treated as independent continuous random variables. The random vector $\boldsymbol{\xi}$, whose dimension is equal to the number of uncertain variables n_ξ, belongs to the probability space $(\Omega, \mathcal{F}, P)$, composed by the sample space Ω, the σ-algebra $\mathcal{F}$ of the subsets of the events, and a probability measure P. It essentially maps the samples in $\Omega = [0, 1]^{n_\xi}$ into the random outcomes $\boldsymbol{\xi} \in \Xi$, and it is characterized by the probability density function $p_\xi(\boldsymbol{\xi})$. The output of the system, *i.e.,* the quantity of interest f_i in our case, is then a stochastic variable.

In the robust optimization procedure, the interest is in reconstructing the mean value and the variance of the quantity of interest; the stochastic output variable is referred to as $f_i(\boldsymbol{x}_\mathbf{s}, \boldsymbol{\xi})$, where $\boldsymbol{x}_s$ is the vector of the design variables. Let us define the expected value of the stochastic variable f_i as follows:

$$\langle f_i \rangle = \int_{\Xi} f_i(\boldsymbol{x}_\mathbf{s}, \boldsymbol{\xi})\ p_\xi(\boldsymbol{\xi})\ \mathrm{d}\xi,$$

with $p_\xi(\boldsymbol{\xi}) = \prod_i^{n_\xi} p_{\xi_i}(\xi_i)$ the joint probability of the independent input variables, and the inner product operator of two stochastic variables f_i and g_i with respect to the joint probability (i.e., the covariance for independent f_i and g_i),

$$\langle f_i, g_i \rangle = \int_{\Xi} f_i(\boldsymbol{x}_\mathbf{s}, \boldsymbol{\xi}) g_i(\boldsymbol{x}_\mathbf{s}, \boldsymbol{\xi})\ p_\xi(\boldsymbol{\xi})\ \mathrm{d}\xi.$$

The mean and variance then read

$$\begin{aligned} \mu(f_i) &= \langle f_i \rangle, \\ \sigma^2(f_i) &= \langle f_i, f_i \rangle - \langle f_i \rangle^2. \end{aligned} \tag{9}$$

To reconstruct the quantities in Eq. (9), a polynomial chaos (PC) expansion method [39] is used. In fact, under specific conditions, a stochastic process can be expressed as a spectral expansion based on suitable orthogonal polynomials, with weights associated with a particular probability density function. The first study in this field is the Wiener process that was later developed in Ref. [39]. The basic idea is to project the variables of the problem onto a stochastic space spanned by a complete set of orthogonal polynomials Ψ that are functions of the random variables $\boldsymbol{\xi}$. For example, variable f_i has the following spectral representation:

$$f_i\ (\boldsymbol{x}_\mathbf{s}, \boldsymbol{\xi}) = \sum_{k=0}^{\infty} \alpha_k\ (\boldsymbol{x}_\mathbf{s})\ \Psi_k\ (\boldsymbol{\xi}) \tag{10}$$

where Ψ_k are the PC orthogonal polynomials, and α_k the coefficients of the expansion. In practice, the series in Eq. (10) has to be truncated to a finite number of terms N, which is determined by

$$N + 1 = \frac{(n_\xi + n_o)!}{n_\xi!\ n_o!}$$

where n_ξ is the dimension of the uncertainty vector $\boldsymbol{\xi}$, and n_o is the order of the univariate polynomial expansion $\phi_i(\xi_i)$ from which the multivariate polynomials $\Psi_k(\boldsymbol{\xi})$ are obtained via tensorization, i.e.,

$$\Psi_k\ (\boldsymbol{\xi}) = \prod_i^{n_\xi} \phi_i(\xi_i).$$

The polynomial basis $\phi_i(\xi_i)$ is chosen according to the Wiener–Askey scheme [39] in order to select orthogonal polynomials with respect to the probability density function $p_\xi(\boldsymbol{\xi})$ of the input. In this work, because a uniform distribution is considered, Legendre polynomials are employed. The orthogonality property can be advantageously used to compute the PC coefficients of the expansion α_k in a non-intrusive PC framework; this procedure is called Non-Intrusive Spectral Projection (NISP) [6]. In fact, from the orthogonality property it directly follows that

$$\alpha_k = \frac{\langle f_i(\boldsymbol{x}_\mathbf{s}, \boldsymbol{\xi}), \Psi_k(\boldsymbol{\xi}) \rangle}{\langle \Psi_k(\boldsymbol{\xi}), \Psi_k(\boldsymbol{\xi}) \rangle} \quad \forall k. \tag{11}$$

The computation of the PC coefficients requires an integration of the polynomials that can be estimated with several approaches, among which quadrature formula are chosen in this study. As a result, the solution of the deterministic problem is required for each quadrature point. Once the polynomial chaos and the associated α_k

Table 12 Summary of robust optimization problems

Case	Objective	Inequality constraints	Design variables
RMO1	$\max(\mu(f_1))$ and $\min(\sigma^2(f_1))$	$\lvert C_M\rvert \leq \overline{C_M}$	$\boldsymbol{x}_{m,c}$
RMO2	$\max(\mu(f_2))$ and $\min(\sigma^2(f_2))$	$\lvert C_M\rvert \leq \overline{C_M}$	$\boldsymbol{x}_{m,c}$

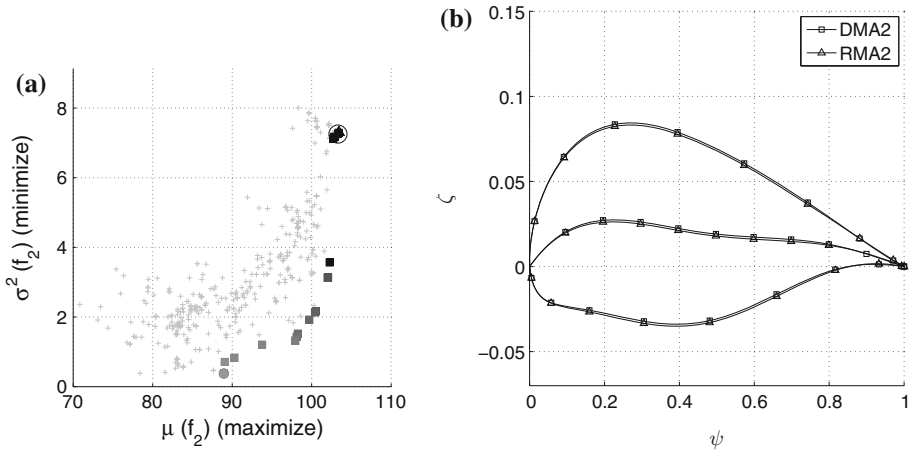

Fig. 11 Results of the robust optimization for the retreating side (RMO2): **a** Pareto front, **b** optimal deterministic and robust airfoils

coefficients are computed, the mean value and the variance of the stochastic solution $f_i\,(\boldsymbol{x}_\mathbf{s}, \boldsymbol{\xi})$ are obtained leveraging the orthogonality of the polynomials Ψ_k with respect to the probability function p_ξ:

$$\mu(f_i)|_{\mathrm{PC}} = \left\langle \sum_{k=0}^{N} \alpha_k\,(\boldsymbol{x}_\mathbf{s})\,\Psi_k\,(\boldsymbol{\xi}) \right\rangle = \alpha_0\,(\boldsymbol{x}_\mathbf{s})\,,$$

$$\sigma^2(f_i)|_{\mathrm{PC}} = \left\langle \left(\sum_{k=0}^{N} \alpha_k\,(\boldsymbol{x}_\mathbf{s})\,\Psi_k\,(\boldsymbol{\xi}) \right)^2 \right\rangle - \alpha_0^2\,(\boldsymbol{x}_\mathbf{s})$$

$$= \sum_{k=1}^{N} \alpha_k^2\,(\boldsymbol{x}_\mathbf{s})\left\langle \Psi_k^2 \right\rangle.$$

Because a uniform distribution is considered also in the forward flight case, Legendre polynomials are employed in the PC expansion. The order of the expansion is retained from a convergence analysis which has been performed and proved that a fourth-order polynomial is sufficient to accurately capture the statistics. The reconstruction of the statistics is based on the evaluation of the exact function for a set of samples $\boldsymbol{\xi}_k$ in the uncertain variables domain for each design vector $\overline{\boldsymbol{x}_s}$.

4.3.3 Results

Two optimization problems are then performed, which are summarized in Table 12.

Given the analysis of the previous sections, the nominal operating conditions are set from the deterministic results. In other words, the nominal operating condition of the robust optimization in the advancing side is defined by the angle of attack $\overline{\alpha_1}$ of airfoil DMA1, while for the retreating side the nominal angle of attack is the angle $\overline{\alpha_2}$ of airfoil DMA2.

In the robust optimization problem (RMO2), the Pareto front shown in Fig. 11a is obtained. To select an interesting airfoil from the Pareto set, the lift coefficient obtained in the samples over the stochastic domain is plotted against the target lift coefficient, and an airfoil is selected from the front. The selected airfoil is plotted in Fig. 11b together with the deterministic airfoil DMA2. This airfoil is referred to as RMA2, and its performance in the uncertainty range around the operating condition satisfying the lift constraint is reported

Table 13 Drag coefficient of the deterministic airfoil minimizing C_{D_2} (DMA2) and the airfoil selected from the robust front in the retreating side (RMA2)

Airfoil	$C_{D,2}\|_{\overline{C_{L_2}}}$ (counts)	$\alpha_1\|_{\overline{C_{L_2}}}$ (°)	$\mu_{C_{D,2}}$ (counts)	$\sigma^2_{C_{D,2}}$ (counts^2)	$(\sigma/\mu)_{C_{D,2}}$ (–)
DMA2	135.6	9.62	135.9	39.99	0.047
RMA2	136.6	9.62	136.7	40.06	0.046

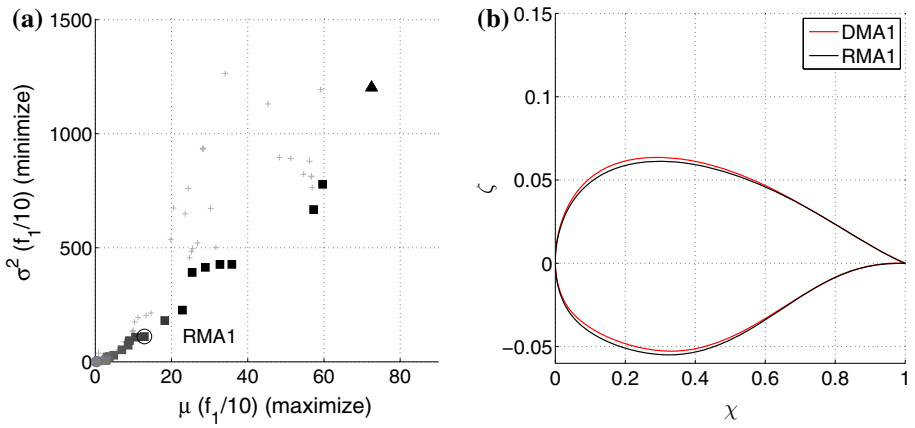

Fig. 12 Results of the robust optimization for the advancing side (RMO1): **a** Pareto front, **b** optimal deterministic and robust airfoils

Table 14 Drag coefficient of the deterministic airfoil minimizing C_{D_1} (DMA1) and the airfoil selected from the robust front in the advancing side (RMA1) with camber morphing

Airfoil	$C_{D,1}\|_{\overline{C_{L_1}}}$ (counts)	$\alpha_1\|_{\overline{C_{L_1}}}$ (°)	$\mu_{C_{D,1}}$ (counts)	$\sigma^2_{C_{D,1}}$ (counts^2)	$(\sigma/\mu)_{C_{D,1}}$ (–)
DMA1	0.805	−0.945	3.99	31.09	1.4
RMA1	0.827	−0.894	5.07	43.57	1.3

in Table 13. It is possible to note that airfoils DMA2 and RMA2 are very similar, and therefore, they present similar performance. In this case, the result from the deterministic optimization is a robust airfoil in itself. However, it is important to note that this in general may not be the case and that robust optimization formulation represents a procedure to guarantee that the optimal airfoils would not incur in lift loss, drag increase or moment penalties throughout the uncertainty range.

The results of the robust optimization problem in the advancing side (RMO1) are shown in Fig. 12a. In the Pareto front, airfoil RMA1 is highlighted which is chosen for its significantly low variance and average mean performance. The shape of airfoil RMA1 is presented in Fig. 12b along with the deterministic optimal airfoil. It is possible to note that even in this case the deterministic solution is very similar to a non-dominated robust airfoil. The deterministic airfoil is also very robust, as demonstrated by the values of the mean and variance presented in Table 14.

5 Validation with azimuth

After evaluating the performance in the advancing and retreating side, the drag coefficient of the optimal airfoils over the azimuth angle of the blade rotation is computed. In the case of a morphing airfoil, a smooth transition from the optimal shape in the advancing side to the optimal shape in the retreating side is required. The transition over the azimuth angle ψ is obtained as follows:

$$\zeta = \frac{\zeta_1}{2}(1 + \sin(\psi)) + \frac{\zeta_2}{2}(1 - \sin(\psi)) \tag{12}$$

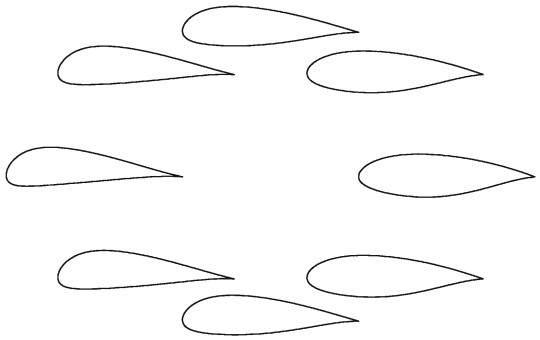

Fig. 13 Shapes over the azimuth obtained by morphing DA1 into DA2

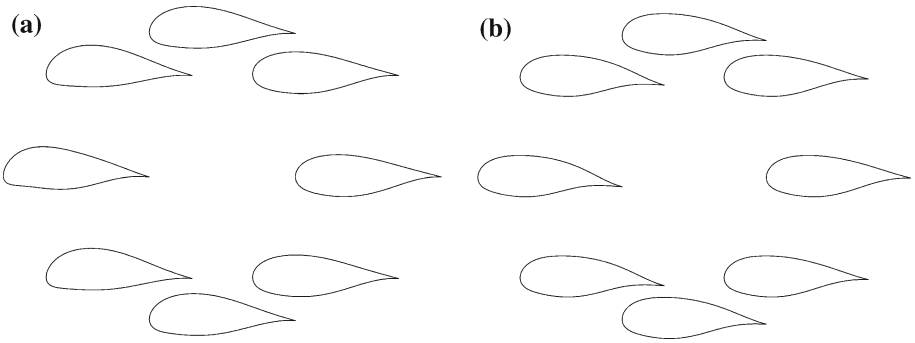

Fig. 14 Shapes over the azimuth: **a** morphing DMA1 into DMA2, **b** morphing DTA1 into DTA2

Table 15 Variables of time-varying angle of attack for optimal shapes

	DA1–DA2	DMA1–DMA2	DTA1–DTA2
α_0 (°)	4.13	4.34	4.49
Δ_1 (°)	4.95	5.10	5.36

Table 16 Average drag coefficient over the blade rotation period for morphing airfoils and associated gain

	DA1–DA2	DMA1–DMA2	DTA1–DTA2
avg(C_D) (counts)	76.44	81.84	95.14
Gain wrt DA0	22.6 %	17.1 %	3.6 %

where ζ_1 is the shape in the advancing side ($\zeta(90°) = \zeta_1$) and ζ_2 is the shape in the retreating side ($\zeta(270°) = \zeta_2$). The transition in the case of the "ideal" morphing DA1-DA2 is presented in Fig. 13, while the morphing shapes with geometrical constraints are shown in Fig. 14. The drag coefficient is then evaluated as follows:

- for the advancing side, an Euler equations simulation with SU^2 is performed, with the setup used in the optimization loop (Sect. 2.2). Because the Euler equations are used, a correction associated with viscous effects is added to the inviscid SU^2 estimate combining the van Driest II method and a form-factor correction as presented in Ref. [17];
- for the retreating side, the XFOIL solver is adopted
- for the remaining intermediate points, the MSES code is used

The values of the mean angle of attack and the first harmonic amplitude are computed and reported in Table 15 for the following combinations: (i) DA1-DA2, i.e., airfoil DA1 morphing into DA2, (ii) DMA1-DMA2, i.e., airfoil DMA1 morphing into DMA2, and (iii) DTA1-DTA2, i.e., airfoil DTA1 morphing into DTA2. The lift and drag coefficients for these airfoils are presented in Fig. 15. It is possible to note that the largest difference among these airfoils is the performance in the retreating side, where the lowest drag coefficient is obtained for the "ideal" morphing, and the drag coefficient increases with increasing geometrical

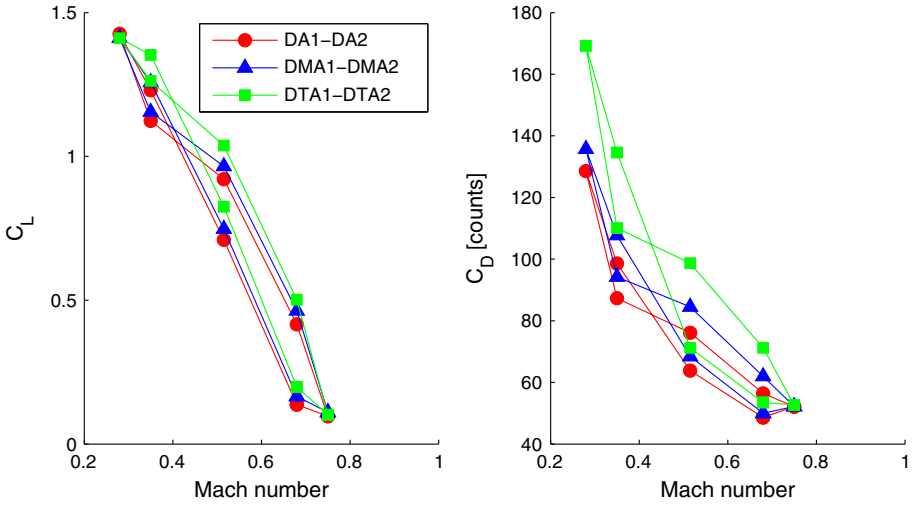

Fig. 15 Lift and drag coefficient loop of DA1–DA2, DMA1–DMA2 and DTA1–DTA2

constraints. The performance in the advancing side is comparable among the different morphing strategies, because the viscous correction [17] is dominant with respect to the inviscid drag coefficient.

The average drag coefficient obtained with the "ideal" morphing and the camber morphing are presented in Table 16. The table also includes the gain with respect to the non-morphing optimal airfoil DA0 which is higher for the ideal case (22.6 %) and reduces to 17.1 and 3 % in the case of the camber morphing and trailing edge modification, respectively. It is clear that to obtain the maximum gain of the morphing strategies an optimization which can model the thickness distribution as well is necessary.

6 Conclusions

A methodology for robust optimization has been developed to tackle the problem of designing morphing airfoils, which could be used for helicopter rotor blades. Robust optimization requires the coupling of the uncertainty quantification method and the optimization algorithm. This coupling increases the computational demand, especially in aerodynamic applications, where a single function evaluation may be very expensive.

Morphing airfoils have been considered as a possible solution to cope with the variable flow conditions encountered by a blade element in forward flight. Deterministic estimates prove that an "ideal" morphing can increase the performance of an optimal non-morphing airfoil by 22.6 % on the average drag coefficient and by 17 % when the thickness constraint is considered.

The employment of robust optimization is thus expected to be of great interest in the application of helicopter rotor airfoils, owing to the fact that even the airfoils with higher mean values achieve lower values of the variance of the aerodynamic efficiency with respect to variations of the angle of attack. The reduction in the variance could lead for instance to a reduction of the required rotor shaft torque in variable operating conditions. Furthermore, in the different applications presented in this paper, results have demonstrated how the robust optimization formulation represents a formal procedure to guarantee that the optimal airfoils would not incur in lift loss, drag increase or moment penalties throughout the uncertainty range.

Future works will be devoted to the unsteady assessment of the morphing geometries to ultimately verify the result of the steady optimization. In addition, an optimization including the thickness distribution as a design variable will be considered for the morphing cases. Building on top of the presented work of an airfoil optimization for two azimuth positions and a single radial station, it is possible to build a more complete framework for rotor optimization, where multiple stations and azimuth angles can be considered. With regard to the robust technique developed in this paper, the joint employment of the multi-fidelity method and coupled adaptive approach will be explored to further improve numerical efficiency.

References

1. Abbott, I.H., von Doenhoff, A.E.: Theory of Wing Section. Dover Publications Inc., New York (1949)
2. Airoldi, A., Crespi, M., Quaranta, G., Sala, G.: Design of a morphing airfoil with composite chiral structure. J. Aircr. **49**(4), 1008–1019 (2012)
3. Bailly, J., Delrieux, Y.: Improvement of noise reduction and performance for a helicopter model rotor blade by active twist actuation. In: Proceedings of 35th European Rotorcraft Forum, Hamburg, Germany, 22–25 Sept (2009)
4. Barbarino, S., Bilgen, O., Ajaj, R.M., Friswell, M.I., Inman, D.J.: A review of morphing aircraft. J. Intell. Mater. Syst. Struct. **22**(9), 823–877 (2011)
5. Bousman, W.G.: Airfoil design and rotorcraft performance. In: American Helicopter Society 58th Annual Forum, Montreal, Canada (2002)
6. Congedo, P., Corre, C., Martinez, J.M.: Shape optimization of an airfoil in a BZT flow with multiple-source uncertainties. Comput. Methods Appl. Mech. Eng. **200**(1–4), 216–232 (2011)
7. De Gaspari, A., Ricci, S.: A two-level approach for the optimal design of morphing wings based on compliant structures. J. Intell. Mater. Syst. Struct. **22**(10), 1091–1111 (2011)
8. Drela, M.: Xfoil: an analysis and design system for low Reynolds number airfoils. Conf. Low Reynolds Number Airfoil Aerodyn. Univ. Notre Dame **54**, 1–12 (1989)
9. Fanjoy, D., Crossley, W.A.: Aerodynamic shape design for rotor airfoils via genetic algorithm. J. Am. Helicopter Soc. **43**(3), 263–270 (1998)
10. Fincham, J., Friswell, M.: Aerodynamic optimisation of a camber morphing aerofoil. Aerosp. Sci. Technol. **43**, 245–255 (2015)
11. Fusi, F., Guardone, A., Quaranta, G., Congedo, P.M.: Multi-fidelity physics-based method for robust optimization with application to a hovering rotor airfoil. AIAA J. **53**(11), 3448–3465 (2015)
12. Gandhi, F., Frecker, M., Nissly, A.: Design optimization of a controllable camber rotor airfoil. AIAA J. **46**(1), 142–153 (2008)
13. Hirsch, C.: Numerical Computation of Internal and External Flows, 2nd edn. Butterworth-Heinemann, Oxford (2007)
14. Johnson, W.: Rotorcraft aerodynamics models for a comprehensive analysis. Technical report, Revised version of paper presented at the American Helicopter Society 54th Annual Forum (1998)
15. Johnson, W.: Rotorcraft dynamics models for a comprehensive analysis. Technical report, Revised version of paper presented at the American Helicopter Society 54th Annual Forum (1998)
16. Johnson, W.: Rotorcraft Aeromechanics. Cambridge University Press, New York (2013)
17. Kenway, G., Martins, J.R.R.A.: Multipoint high-fidelity aerostructural optimization of a transport aircraft configuration. J. Aircr. **51**(1), 144–160 (2014)
18. Kerho, M.F.: Adaptive airfoil dynamic stall control. J. Aircr. **44**(4), 1350–1360 (2007)
19. Kottapalli, S.: Low speed and high speed correlation of smart active flap rotor loads. In: American Helicopter Society Specialists Conference on Aeromechanics (2010)
20. Kulfan, B.M., Bussoletti, J.E.: "Fundamental" parametric geometry representations for aircraft component shapes. In: 11th AIAA/ISSMO Multidisciplinary Analysis and Optimization Conference, Portsmouth, VA (2006)
21. Lee, D.S., Periaux, J., Onate, E., Gonzalez, L.F., Qin, N.: Active transonic aerofoil design optimization using robust multi-objective evolutionary algorithms. J. Aircr. **48**(3), 1084–1094 (2011)
22. Leishman, J.G.: Principles of Helicopter Aerodynamics. Cambridge University Press, Cambridge (2006)
23. Mäkinen, R.A.E., Periaux, J., Toivanen, J.: Shape design optimization in 2D aerodynamics using genetic algorithms on parallel computers. In: Taylor, S., Ecer, A., Periaux, J., Satofuka, N. (eds.) Parallel Computational Fluid Dynamics, pp. 395–402. Elsevier, Amsterdam (1995)
24. Martin, P.B., McAlister, K., Chandrasekhara, M.S., Geissler, W.: Dynamic stall measurements and computations for a vr-12 airfoil with a variable droop leading edge. In: 59th Annual Forum of the American Helicopter Society, Phoenix, Arizona, 6–8 May (2003)
25. Masarati, P., Morandini, M., Mantegazza, P.: An efficient formulation for general-purpose multibody/multiphysics analysis. J. Comput. Nonlinear Dyn. **9**(4), 041,001 (2014)
26. Masarati, P., Piatak, D.J., Quaranta, G., Singleton, J.D., Shen, J.: Soft-inplane tiltrotor aeromechanics investigation using two comprehensive multibody solvers. J. Am. Helicopter Soc. **53**(2), 179–192 (2008)
27. Massaro, A., Benini, E.: Multi-objective optimization of helicopter airfoils using surrogate-assisted memetic algorithms. J. Aircr. **49**(2), 375–383 (2012)
28. Morris, A., Allen, C., Rendall, T.: Aerodynamic optimisation of hovering helicopter rotors using efficient and flexible shape parameterisation. In: 26th AIAA Applied Aerodynamics Conference (2008)
29. Mura, G.L., Qin, N.: Local class shape transformation parameterization (I-CST) for airfoils. In: American Institute of Aeronautics and Astronautics (2017)
30. Murugan, M.S., Woods, B.K.S., Friswell, M.I.: Morphing helicopter rotor blade with curvilinear fiber composites. In: 38th European Rotorcraft Forum (2012)
31. Murugan, S., Chowdhury, R., Adhikari, S., Friswell, M.: Helicopter aeroelastic analysis with spatially uncertain rotor blade properties. Aerosp. Sci. Technol. **16**(1), 29–39 (2012)
32. Murugan, S., Woods, B., Friswell, M.: Hierarchical modeling and optimization of camber morphing airfoil. Aerosp. Sci. Technol. **42**, 31–38 (2015)
33. Palacios, F., Colonno, M.R., Aranake, A.C., Campos, A., Copeland, S.R., Economon, T.D., Lonkar, A., Lukaczyk, T.W., Taylor, T.W.R., Alonso, J.J.: Stanford University Unstructured (SU2): an open-source integrated computational environment for multi-physics simulation and design. In: 51st AIAA Aerospace Sciences Meeting including the New Horizons Forum and Aerospace Exposition (2013)

34. Palacios, F., Economon, T.D., Aranake, A.C., Copeland, S.R., Lonkar, A.K., Lukaczyk, T.W., Manosalvas, D.E., Naik, K.R., Padron, A.S., Tracey, B., Variyar, A., Alonso, J.J.: Stanford University Unstructured (SU2): open-source analysis and design technology for turbulent flows. In: 52nd Aerospace Sciences Meeting (2014)
35. Potsdam, M., Fulton, M.V., Dimanlig, A.: Multidisciplinary cfd/csd analysis of the smart active flap rotor. In: 66th Annual Forum of the American Helicopter Society, Phoenix, Arizona, 11–13 May (2010)
36. Srinivas, N., Deb, K.: Multiobjective function optimization using nondominated sorting genetic algorithms. Evol. Comput. **2**(3), 221–248 (1994)
37. Trenker, M.: Design concepts for adaptive airfoils with dynamic transonic flow control. J. Aircr. **40**(4), 734–740 (2003)
38. van der Wall, B.G.: 2nd HHC Aeroacoustic Rotor Test (HART II)—Part I: Test Documentation. DLR, Braunschweig (2003)
39. Xiu, D., Karniadakis, G.E.: The Wiener–Askey polynomial chaos for stochastic differential equations. SIAM J. Sci. Comput. **24**(2), 619–644 (2002)
40. Zanotti, A., Nilifard, R., Gibertini, G., Guardone, A., Quaranta, G.: Assessment of 2D/3D numerical modeling for deep dynamic stall experiments. J. Fluids Struct. **51**(1), 97–115 (2014)
41. Zhang, Q., Hoffmann, F.: Benefit studies for rotor with active twist control using weak fluid-structure coupling. In: Proceedings of 35th European Rotorcraft Forum, Hamburg, Germany, 22–25 Sept (2009)